

Microwave spectrometry for the evaluation of the structural integrity of metallic stents

Gianluca Arauz-Garofalo, Víctor López-Domínguez, Joan Manel Hernández, Oriol Rodríguez-Leor, Antoni Bayés-Genís, Juan M. O'Callaghan, Antoni García-Santiago, and Javier Tejada

Citation: *Medical Physics* **41**, 041902 (2014); doi: 10.1118/1.4866881

View online: <http://dx.doi.org/10.1118/1.4866881>

View Table of Contents: <http://scitation.aip.org/content/aapm/journal/medphys/41/4?ver=pdfcov>

Published by the [American Association of Physicists in Medicine](#)

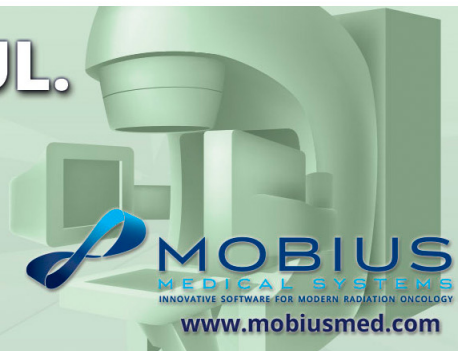
FAST. SIMPLE. POWERFUL.

AUTOMATE YOUR TG-142 QA AND SAVE HOURS OF TIME



DoseLab

THE FIRST QA SOFTWARE TO GET TG-142 RIGHT



Microwave spectrometry for the evaluation of the structural integrity of metallic stents

Gianluca Arauz-Garofalo^{a)} and Víctor López-Domínguez

Grup de Magnetisme, Departament de Física Fonamental, Facultat de Física, Universitat de Barcelona, Martí i Franquès 1, planta 4, edifici nou, ES-08028 Barcelona, Spain

Joan Manel Hernández

Grup de Magnetisme, Departament de Física Fonamental, Facultat de Física, Universitat de Barcelona, Martí i Franquès 1, planta 4, edifici nou, ES-08028 Barcelona, Spain and Institut de Nanociència i Nanotecnologia IN2UB, Universitat de Barcelona, Martí i Franquès 1, planta 3, edifici nou, ES-08028 Barcelona, Spain

Oriol Rodríguez-Leor and Antoni Bayés-Genís

Servei de Cardiologia, Hospital Universitari Germans Trias i Pujol, Carretera del Canyet s/n, ES-08916 Badalona, Spain

Juan M. O'Callaghan

Department of Signal Theory and Communications, Universitat Politècnica de Catalunya, Jordi Girona 1, ES-08034 Barcelona, Spain

Antoni García-Santiago^{b)} and Javier Tejada

Grup de Magnetisme, Departament de Física Fonamental, Facultat de Física, Universitat de Barcelona, Martí i Franquès 1, planta 4, edifici nou, ES-08028 Barcelona, Spain and Institut de Nanociència i Nanotecnologia IN2UB, Universitat de Barcelona, Martí i Franquès 1, planta 3, edifici nou, ES-08028 Barcelona, Spain

(Received 5 June 2013; revised 5 February 2014; accepted for publication 10 February 2014; published 5 March 2014)

Purpose: To assess the feasibility of a method based on microwave spectrometry to detect structural distortions of metallic stents in open air conditions and envisage the prospects of this approach toward possible medical applicability for the evaluation of implanted stents.

Methods: Microwave absorbance spectra between 2.0 and 18.0 GHz were acquired in open air for the characterization of a set of commercial stents using a specifically design setup. Rotating each sample over 360°, 2D absorbance diagrams were generated as a function of frequency and rotation angle. To check our approach for detecting changes in stent length (fracture) and diameter (recoil), two specific tests were performed in open air. Finally, with a few adjustments, this same system provides 2D absorbance diagrams of stents immersed in a water-based phantom, this time over a bandwidth ranging from 0.2 to 1.8 GHz.

Results: The authors show that metallic stents exhibit characteristic resonant frequencies in their microwave absorbance spectra in open air which depend on their length and, as a result, may reflect the occurrence of structural distortions. These resonances can be understood considering that such devices behave like dipole antennas in terms of microwave scattering. From fracture tests, the authors infer that microwave spectrometry provides signs of presence of Type I to Type IV stent fractures and allows in particular a quantitative evaluation of Type III and Type IV fractures. Recoil tests show that microwave spectrometry seems able to provide some quantitative assessment of diametrical shrinkage, but only if it involves longitudinal shortening. Finally, the authors observe that the resonant frequencies of stents placed inside the phantom shift down with respect to the corresponding open air frequencies, as it should be expected considering the increase of dielectric permittivity from air to water.

Conclusions: The evaluation of stent resonant frequencies provided by microwave spectrometry allows detection and some quantitative assessment of stent fracture and recoil in open air conditions. Resonances of stents immersed in water can be also detected and their characteristic frequencies are in good agreement with theoretical estimates. Although these are promising results, further verification in a more relevant phantom is required in order to foresee the real potential of this approach.

© 2014 American Association of Physicists in Medicine. [<http://dx.doi.org/10.1118/1.4866881>]

Key words: microwaves, stents, coronary artery disease, stent fracture, stent recoil

1. INTRODUCTION

A stent^{1,2} is a medical prosthetic device shaped as a small cylindrical tube with wire mesh walls, which is used to

revascularize atherosclerotic stenosed blood vessels. The first generation of conventional, bare-metal stents was developed in the mid-1980s.³ Despite their obvious advantages, in-stent neointimal hyperplasia⁴⁻⁶ occurred in some cases. This

phenomenon, also known as in-stent restenosis, was directly linked to stent implantation and resulted in restenosis rates of 20%–30%.⁷ It was the attempt to minimize this problem, and thereby reduce rates of repeated revascularization, that ultimately lead to the development of drug-eluting stents.⁸ The dramatic reduction in restenosis rates seen with the use of this second generation as compared with the first one^{9–13} has been the major driving force behind the exponential growth of percutaneous coronary interventions as a treatment for patients with coronary artery disease. However, even with such improvements, patients with coronary stents require chronic medication and monitoring in order to prevent restenosis and deterioration of the stent structural integrity.

In particular, physicians have studied the contributing factors and the clinical effects of stent fracture and stent recoil in veins, coronary, and noncoronary arteries. Even if fracture does not necessarily involve clinical sequelae, it represents a risk factor for restenosis, target lesion revascularization, and other complications such as thrombosis, myocardial infarction, and even sudden cardiac death.^{14–26} Extensive studies quantifying the true incidence of stent fracture continue to be lacking. Reported values range from 0.84% (Ref. 27) to 65.4% (Ref. 28), although most of the available literature gives numbers below 8%. Some authors have explicitly pointed out the lack of routine methods of monitoring or diagnosing stent fractures²⁹ as well as the importance of detecting this phenomenon before the onset of related symptoms.²⁵ Conversely, stent recoil has been much less studied, but in any case its presence has been linked with unsatisfactory revascularization and therefore with an increased risk of adverse events.^{30–34} A few studies give incidence values from 1.6% to 6.9% and state that recoil is a significant phenomenon that should be further explored.^{33,34}

For all these reasons considerable effort has been made to improve stenting outcome. On the one hand, research has been carried out to improve the design of stents. Promising examples are biodegradable stents³⁵ or devices allowing wireless monitoring of pressure and blood flow.^{36,37} Manufacturing methods based on microelectrodischarge machining have also been suggested.³⁸ On the other hand, work is being conducted for the optimization of medical imaging techniques aiming to produce real-time high-quality images with minimal damage to the patient. These include noninvasive techniques such as magnetic resonance³⁹ and duplex ultrasound,⁴⁰ as well as invasive methods such as x-ray angiography,⁴¹ intravascular ultrasound,⁴² intravascular photoacoustic imaging,⁴³ and optical coherence tomography.⁴⁴ In spite of the obvious clinical benefits, these techniques require justification of potential patient collateral damages, such as impact of invasive procedures or ionizing radiation dose. Microwave-based techniques have the advantage of being nonionizing and noninvasive, and that is why they are particularly suitable to develop new medical applications.⁴⁵

We assess the feasibility of a method based upon microwave spectrometry (MWS) to detect structural distortions of metallic stents. We show here that such devices exhibit characteristic resonant frequencies in their microwave absorbance spectra which reflect the occurrence of changes in

stent length (fracture) or diameter (recoil), at least in open air conditions. These resonant frequencies are also detected when the stents are immersed in water and their values are in good agreement with theoretical estimates. Further verification in a more physiologically relevant phantom is required in order to evaluate MWS as a possible new medical tool to improve the monitoring of patients with implanted metallic stents.

2. EXPERIMENTAL METHODS

The experimental methods developed present three separate stages. In the first part, we used MWS to characterize a set of stents with the aim of achieving a global understanding of the fundamental processes involved in the interaction of microwaves with such devices. In the second part, only a few stents with controlled structural distortions were tested for the purpose of checking the capabilities of MWS to detect stent fracture and recoil. Finally, in order to foresee the medical applicability of MWS, the study conducted in the first part was reproduced, but this time using a more reliable environment such as a water-based phantom.

2.A. Samples

We performed this study on 75 coronary stents of six different models from a single brand (see Table I). All of them were fabricated by Medtronic Inc. using a 0.091-mm-thick round wire of an alloy composed by Ni, Co, Cr, and Mo (35%, 32%, 20%, and 10%, respectively) and other elements like Fe, Ti, Mn, Si, and C in ratios lesser than 1%.^{46–50} For each model the manufacturer provides a range of nominal lengths, ℓ_{nom} , and nominal diameters, d_{nom} . The nominal sizes of a given stent are reached expanding the balloon catheter⁵¹ in which it is mounted up to a certain value of nominal inflation pressure, p_{nom} , provided by the manufacturer in its commercial kit. All pressures were achieved and measured by means of a compatible inflation device.⁵² Five models present an architecture composed by a certain number of modular elements (see microphotograph⁵³ in Fig. 1). These modules are shaped as sinusoidal 7-pointed crowns for $d_{\text{nom}} = 2.25\text{--}2.75$ mm and 10-pointed crowns for $d_{\text{nom}} = 3.00\text{--}4.50$ mm. The remaining model is a single wire bent into a continuous sinusoidal architecture. In both cases the structure is reinforced by helicoidal laser-fused welding patterns.

TABLE I. Type, architecture, and number of stents measured for the six models investigated: Driver Sprint (MDS), Integrity (MI), Driver (MD), Micro-Driver (MMD), Endeavor Sprint (MES), and Endeavor Resolute (MER).

Model	Type	Architecture	Stents
MDS	Bare-metal	Modular	31
MI	Bare-metal	Continuous	6
MD	Bare-metal	Modular	3
MMD	Bare-metal	Modular	3
MES	Zotarolimus-eluting	Modular	29
MER	Zotarolimus-eluting	Modular	3

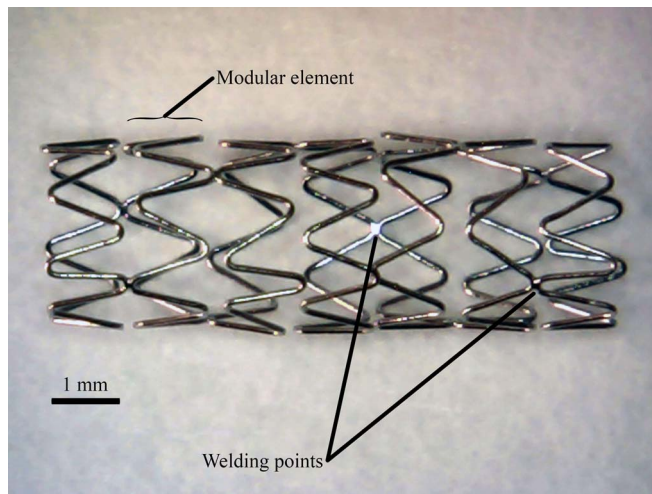


FIG. 1. Microphotograph of a MMD bare-metal stent ($\ell_{\text{nom}} = 8.00$ mm and $d_{\text{nom}} = 2.75$ mm) expanded up to $p_{\text{nom}} = 0.91 \pm 0.05$ MPa. This stent is composed by seven modular elements shaped as 7-pointed sinusoidal crowns held together by means of a single-helix welding pattern.

2.B. Setups

The stents were characterized by measuring their microwave absorbance spectrum using a specifically designed system. Figure 2(a) shows a sketch of the MWS setup used in open air conditions (Setup#1). To carry out the characterizations a pair of microwave antennas with a 2.0–18.0 GHz spectral range⁵⁴ was connected to a two-port vector network analyzer⁵⁵ via coaxial feed lines.⁵⁶ Measurements were performed in a symmetrical configuration in which the center of the stent was placed at the midpoint of the line joining the antennas (optical axis), which were set at a constant separation of 16.0 cm. The stents were positioned with the aid of a handmade expanded polystyrene sample holder mounted on a unipolar stepping motor,⁵⁷ which was connected to a single-board microcontroller⁵⁸ through a home-built circuit. This motorized sample holder allows rotation of the stent longitudinal axis (stent axis) an azimuthal angle φ around a vertical axis that is perpendicular to the optical axis [see the inset in Fig. 2(a)]. The microcontroller and the network analyzer were connected to a computer, and the whole system was controlled by means of a homemade program.⁵⁹ This setup provides the transmission coefficient between the two ports of the network analyzer as a function of frequency, $S(f)$, from which the absorbance spectrum can be calculated as

$$A(f) = 10 \log \left(\frac{S_{\text{ref}}(f)}{S(f)} \right). \quad (1)$$

Here, $S_{\text{ref}}(f)$ denotes the reference transmission coefficient acquired as a function of frequency without any stent placed on the sample holder. Both $S(f)$ and $S_{\text{ref}}(f)$ are the average of one hundred measurements of each magnitude. For every stent subsequent absorbance spectra were obtained in steps of 1.8° over a 360.0° rotation around the vertical axis. All the spectra collected this way for different azimuthal angles are presented in a single absorbance diagram, $A(f, \varphi)$, using graphing and data analysis software.⁶⁰

Figure 2(b) shows a sketch of the phantom used to characterize the stents in a tissuelike environment (Setup#2). It was built as a poly(methyl methacrylate) box ($20 \times 10 \times 9$ cm³) entirely filled with distilled water. Now the antennas were 19.7 cm apart and were embedded in the two farthest opposite faces of the box. In this configuration, the nominal spectral range of the antennas shifts down with respect to the range in open air and becomes around 0.2–1.8 GHz due to the higher permittivity of water.⁶¹ The samples were placed using a slightly modified version of the same rotating sample holder. This time, the stents were threaded through using a 0.30-mm-thick nylon filament, and were suspended from above at the center of the optical axis. As a result, an $A(f, \varphi)$ diagram was obtained for each stent characterized. Data processing and any other system component are identical to those explained for the characterization in open air.

2.C. Microwave resonance in open air

The $A(f, \varphi)$ diagrams in open air were acquired for the full set of stents using Setup#1 as described in Subsection 2.B. All the stents were expanded using their catheters. After completing the expansion and the subsequent $A(f, \varphi)$ acquisition, the real length, ℓ , and the real diameter, d , of each stent were recorded using a digital caliper.⁶² The final value of each magnitude was the average of 12 measurements. The resonant frequencies of every stent were obtained applying peak analysis tools⁶⁰ to the corresponding $A(f, \varphi)$ diagram. To analyze the dependence of such frequencies on the size of the stents, we focused on a subset of 31 [MDS (Ref. 46)] plus 29 [MES (Ref. 49)] samples (see Table II). These two models were selected since they present the widest range of nominal sizes ($\ell_{\text{nom}}, d_{\text{nom}}$) among those available for this study.

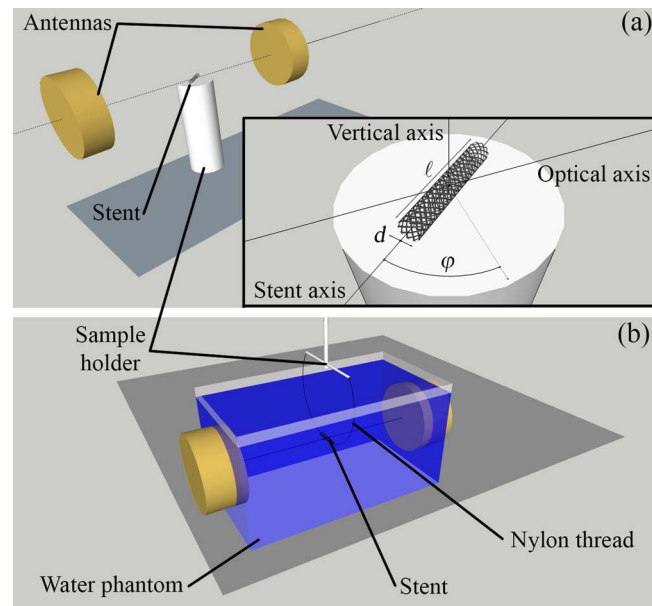


FIG. 2. (a) Sketch of the experimental setup for the microwave characterization of stents in open air conditions (Setup#1). The inset shows a detail of the geometrical configuration. (b) Sketch of the phantom for the microwave characterization of stents in water (Setup#2).

TABLE II. Set of commercial available sizes for the MDS bare-metal stent and the MES Zotarolimus-eluting stent. Horizontal and vertical numbers indicate, respectively, nominal length (ℓ_{nom}) and nominal diameter (d_{nom}), both in millimeters. Solid circles (●) denote the 29 MDS plus 31 MES stents for which the first two resonant frequencies were determined from absorbance diagrams acquired in open air. The three asterisked samples (●*) were damaged in fracture tests and could not be characterized in the subsequent phantom tests. Open circles (○) indicate stents that were not available for analysis in this study.

(mm)	ℓ_{nom}	8.00	9.00	12.00	14.00	15.00	18.00	24.00	30.00
d_{nom}	MDS								
2.25		●		●	●		○	○	○
2.50		●		●●	●		●	●	○
2.75		○		●	●		●	●*	○
3.00			●	○		○	●	○	○
3.50			●	●		●	●	○	●
4.00			●	○		●	●	●	●
4.50			●	●		●	●	●	●
(mm)	ℓ_{nom}	8.00	9.00	12.00	14.00	15.00	18.00	24.00	30.00
d_{nom}	MES								
2.25		●		●	●		○	●	●
2.50		○		●	●		●	●	●*
2.75		○		●	○		○	●	○
3.00			●	●		●	●	●	●
3.50			●	●		●	●	●	●
4.00			○	●		●	●	●	●*

2.D. Fracture tests

We performed fracture tests on two MES stents⁴⁹ ($\ell_{\text{nom}} = 30.00$ mm for both, $d_{\text{nom}} = 2.75$ and 4.00 mm, respectively) and one MDS stent⁴⁶ ($\ell_{\text{nom}} = 24.00$ mm, $d_{\text{nom}} = 2.75$ mm), which were chosen among the subset of MES and MDS stents mentioned in Subsection 2.C. To illustrate the results we have selected the last one, which was originally expanded up to $p_{\text{nom}} = 0.91 \pm 0.05$ MPa. This stent has a modular architecture that is composed by twenty 7-pointed crowns held together by means of a single-helix welding pattern [dark dots in Fig. 3(a)] supported by four extra welds at the ends of the stent [light dots in Fig. 3(a)]. The stent was submitted to a series of four cuts using a customized precision plier and a hand lens. The cutting sequence described below was devised to make the stent go gradually through four of the five stages currently accepted by medical doctors to grade stent fractures.^{28,63} Cut 1 was carried out on the strut close to the weld between crowns #11 and #12 [see small dotted circle in Fig. 3(b)]. As a result the stent presented a single strut fracture (Type I). Cut 2 was executed on the strut near the weld that holds together crowns #5 and #6 [see small dotted circle in Fig. 3(c)]. Hence the stent presented multiple strut fractures (Type II). Cut 3 was performed again on crown #12, in the strut just beneath the one where Cut 1 had been done. This resulted in a complete transverse linear rupture (Type III fracture) that separated the stent in two segments (labeled, respectively, AB and C) [see Fig. 3(d)]. In a similar manner, Cut 4 was applied on crown #6 in segment AB. Thus the stent presented two complete transverse linear fractures (Type IV) that split it in three segments (labeled, respectively, A, B, and

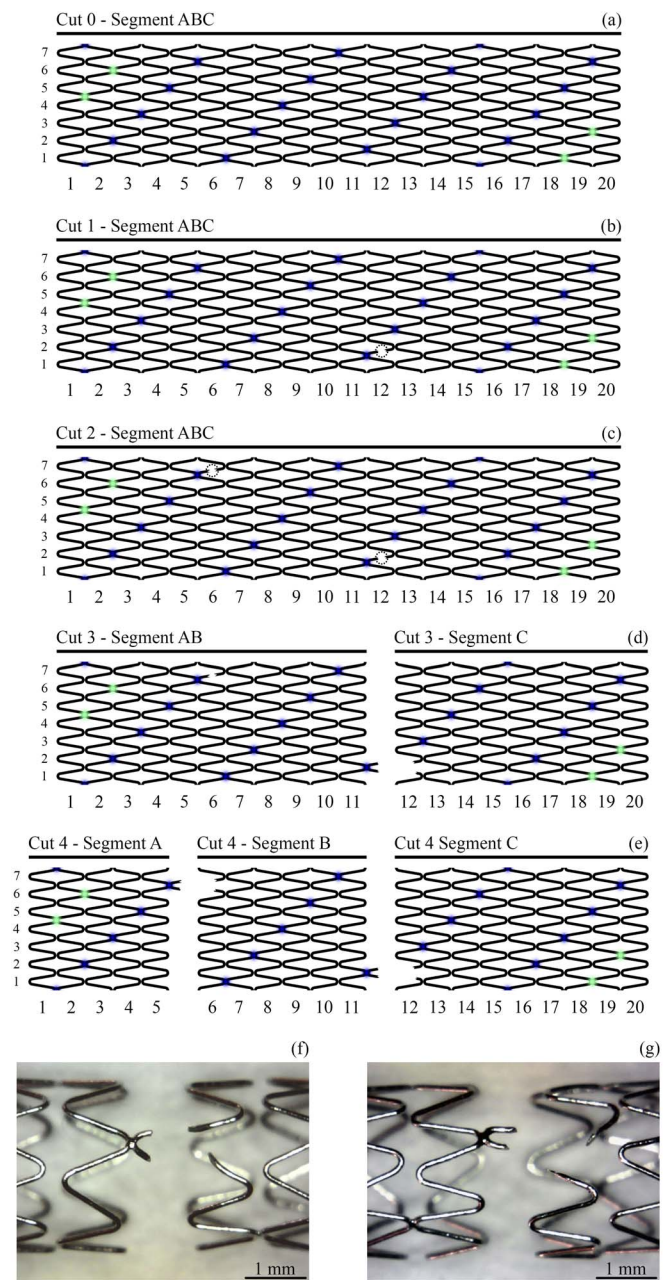


FIG. 3. (a) Planar representation of the modular architecture of a MDS bare-metal stent ($\ell_{\text{nom}} = 24.00$ mm and $d_{\text{nom}} = 2.75$ mm) expanded up to $p_{\text{nom}} = 0.91 \pm 0.05$ MPa. [(b)–(e)] Sequence of four cuts applied to make the stent go through Types I, II, III, and IV fracture grades, respectively. [(f) and (g)] Microphotographs of the regions where Cut 2 and Cut 4, and Cut 1 and Cut 3 were, respectively, performed.

C) [see Fig. 3(e)]. Microphotographs in Fig. 3 detail the final look of the regions on which cuts were made. Figure 3(f) shows the region of Cut 2 and Cut 4, while Fig. 3(g) depicts the region of Cut 1 and Cut 3. After each cut just described, ℓ and d were measured, and $A(f, \varphi)$ diagrams were recorded. The gap between the segments obtained after Cut 3 and Cut 4 [see Figs. 3(d) and 3(e), respectively] was set at 1 mm before the absorbance diagram was acquired for each set of segments. Identical results were obtained with 1, 2, 5, and 10 mm gaps, for the stent shown in Fig. 3 and for the two MES stents mentioned at the beginning of this subsection.

2.E. Recoil tests

We performed recoil test on two MER stents⁵⁰ ($\ell_{\text{nom}} = 15.00$ mm, $d_{\text{nom}} = 3.00$ mm; $\ell_{\text{nom}} = 12.00$ mm, $d_{\text{nom}} = 4.00$ mm), and two MI stents⁴⁷ ($\ell_{\text{nom}} = 26.00$ mm for both, $d_{\text{nom}} = 2.50$ and 2.75 mm, respectively). To exemplify the results we have picked the last one, whose architecture comprises a single wire bent into a continuous sinusoid. The stent was submitted to a stepwise reverse recoil procedure that consisted of a smooth augmentation of d achieved by means of a progressive raise of p using its balloon catheter. Although this goes the way opposite to natural recoil, in which the stent diameter is reduced, we followed this procedure for practical reasons: the balloon catheter is devised to be used to inflate (not to collapse) the stent, and this makes the diameter increase in a uniform way along the whole length of the stent. At each stage, p , d , and ℓ were measured and the corresponding $A(f, \varphi)$ diagram was acquired. To quantify the recoil degree we define the following parameter as a function of d :

$$r(d) = \frac{d_M - d}{d_M - d_m}, \quad (2)$$

where d_M and d_m are the maximum and minimum values for the stent deployment diameter. We chose the diameter at $p_m = 0.00$ MPa (no pressure applied, that is when the stent was just unpacked from its commercial kit) as $d_m = 1.14 \pm 0.05$ mm, and the diameter reached overexpanding the stent up to $p_M = 1.42 \pm 0.05$ MPa as $d_M = 3.29 \pm 0.02$ mm. In this respect, the recoil degree shall be maximum ($r = 1$) for a completely deflated stent ($p = p_m$) and shall be minimum ($r = 0$) for a stent expanded to the maximum pressure value ($p = p_M$) applied in the recoil test. The p_M value for this stent is higher than its corresponding nominal inflation pressure, p_{nom}

$= 0.91 \pm 0.05$ MPa, but in any case is within the safety range given by the manufacturer.⁵⁰

2.F. Microwave resonance in a water phantom

The $A(f, \varphi)$ diagrams of 30 [MDS (Ref. 46)] plus 27 [MES (Ref. 49)] stents (see Table II) immersed in the phantom previously described in Subsection 2.B (Setup#2) were acquired. This was the same subset of stents characterized in open air, except for the three stents that were damaged in fracture tests. The corresponding resonant frequencies were recorded following a procedure analogous to the one previously described in Subsection 2.C and were compared with the values expected from theoretical predictions.

3. RESULTS

3.A. Microwave resonance in open air

To highlight the resonances present in a typical $A(f, \varphi)$ diagram we have chosen a MI stent,⁴⁷ with $\ell_{\text{nom}} = 26.00$ mm and $d_{\text{nom}} = 2.50$ mm. This stent was expanded up to 2.23 ± 0.05 MPa of inflation pressure, p , using the corresponding balloon catheter. Figure 4(a) shows such $A(f, \varphi)$ diagram. Each horizontal line (or isoangular profile) in this graph represents the absorbance spectrum for a given azimuthal angle, $A(f)$, while each vertical line (or isofrequencial profile) represents the absorbance angular pattern for a given frequency, $A(\varphi)$. The isoangular projections show several discrete resonant frequencies [see peaks at $f_1 = 2.55 \pm 0.17$ GHz, $f_2 = 4.87 \pm 0.17$ GHz, and $f_3 = 7.00 \pm 0.17$ GHz in Fig. 4(b), where $A(f)$ spectra are shown for $\varphi = 180^\circ$ and $\varphi = 243^\circ$], each one having characteristic $A(\varphi)$ patterns in its corresponding isofrequencial projection [see Fig. 4(c)]. Such patterns are better identified when $A(\varphi)$ is plotted in polar form, as in Fig. 4(d).

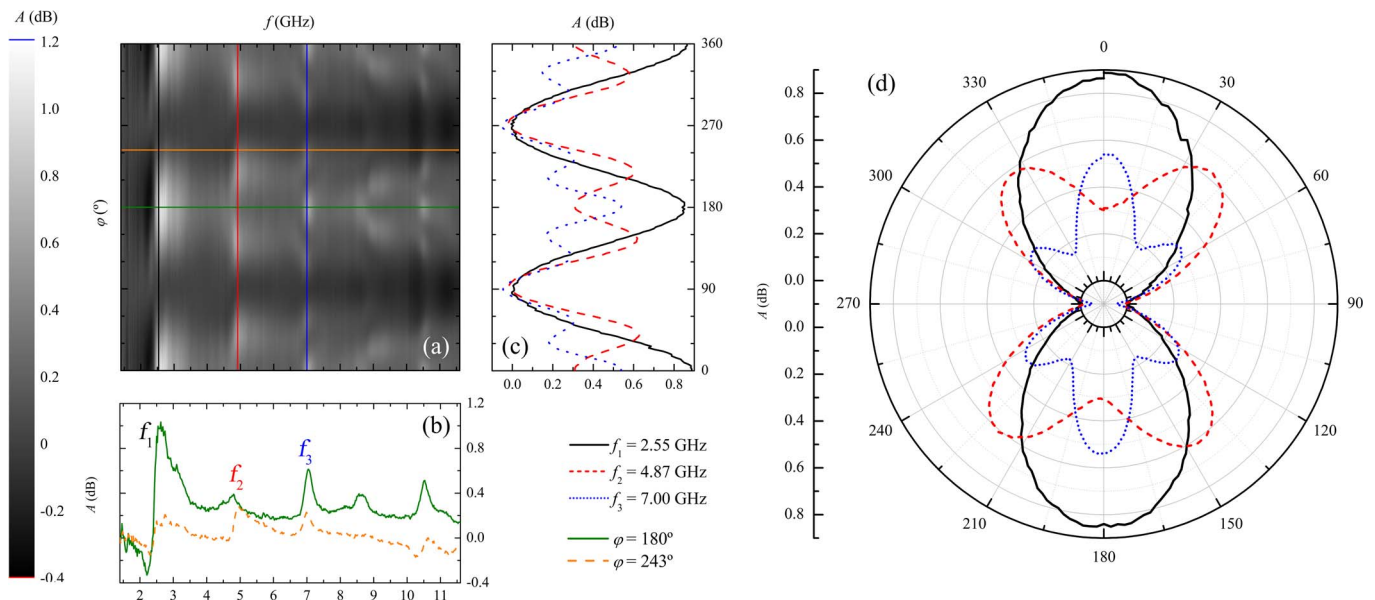


FIG. 4. (a) $A(f, \varphi)$ diagram acquired in open air for a MI bare-metal stent ($d_{\text{nom}} = 2.50$ mm and $\ell_{\text{nom}} = 26.00$ mm) expanded up to $p = 2.23 \pm 0.05$ MPa. (b) Isoangular projections of $A(f, \varphi)$ at $\varphi = 180^\circ$ (solid line) and $\varphi = 243^\circ$ (dashed line). (c) Isofrequencial projections of $A(f, \varphi)$ at $f_1 = 2.55 \pm 0.17$ GHz (solid line), $f_2 = 4.87 \pm 0.17$ GHz (dashed line), and $f_3 = 7.00 \pm 0.17$ GHz (dotted line). (d) Same isofrequencial projections represented in polar form.

The first order, f_1 , shows a bilobular $A(\varphi)$ pattern with peaks occurring when the stent axis is perpendicular to the optical axis. The second order, f_2 , shows a tetralobular $A(\varphi)$ pattern, with four peaks located around 40° , 140° , 220° , and 320° . Higher resonances show more complex $A(\varphi)$ dependences, like hexalobular patterns for the third order, f_3 . We can thus determine the order of a given resonance just inspecting its corresponding $A(\varphi)$ pattern. All the stents characterized in the present work show exactly these same features. Although up to sixth order resonances were identified in some isoangular profiles, the monitoring of f_1 is enough to illustrate our next results.

Figure 5 shows f_1 as a function of ℓ for several d_{nom} values, for the selected subset (see Table II) of 31 MDS stents [Fig. 5(a)] and 29 MES stents [Fig. 5(b)]. All these stents were expanded up to $p_{\text{nom}} = 0.91 \pm 0.05$ MPa using their catheters. Although a well-defined dependence of f_1 on the stent diameter was not found, f_1 seems to follow a $1/\ell$ behavior [interested readers can refer to the supplementary material⁶⁴ for extra figures showing the dependences for $f_1(d)$ and $f_2(\ell)$, in which the same $1/\ell$ behavior can be observed for $f_2(\ell)$].

3.B. Fracture tests

The results for the fracture test performed on the MDS stent with $\ell_{\text{nom}} = 24.00$ mm and $d_{\text{nom}} = 2.75$ mm, expanded up to $p_{\text{nom}} = 0.91 \pm 0.05$ MPa, are shown in Fig. 6 (Type I and Type II stages) and Fig. 7 (Type III and Type IV stages). Table III summarizes the data retrieved from this test. Figures 6(a)–6(c) present the evolution of the $A(f, \varphi)$ diagrams from the intact stent to a Type II fractured stent. Beside the diagrams, the planar representation of the stent geometrical architecture in Figs. 6(d)–6(f) describes the cut sequence applied. The resonant frequencies and the angular patterns present in all diagrams are consistent with the properties reported in Subsection 3.A. Figures 7(a) and 7(d) present, respectively, the same $A(f, \varphi)$ diagram and planar representation of the unaltered stent shown in Figs. 6(a) and 6(d), while Figs. 7(b) and 7(c) represent, respectively, the $A(f, \varphi)$ diagrams for Type III [Fig. 7(e)] and Type IV [Fig. 7(f)] fractures performed on this stent.

3.C. Recoil tests

A selection of steps for the recoil test performed on the MI stent with $\ell_{\text{nom}} = 26.00$ mm and $d_{\text{nom}} = 2.75$ mm is shown in Fig. 8. Figure 8(a) presents the $A(f, \varphi)$ diagram for the stent without recoil, while Figs. 8(b)–8(e) do the same for four increasing recoil degrees, from $r = 0.053 \pm 0.013$ to $r = 0.288 \pm 0.012$. Notice how both f_1 and f_2 shift up progressively from Fig. 8(a) to Fig. 8(e), because as r increases, and so the stent diameter narrows, its length also shortens, and this is finally reflected as a rise of the resonant frequencies in $A(f, \varphi)$. Figure 9 highlights this frequency upshift for the entire recoil test by plotting both f_1 and f_2 as a function of the recoil degree, r .

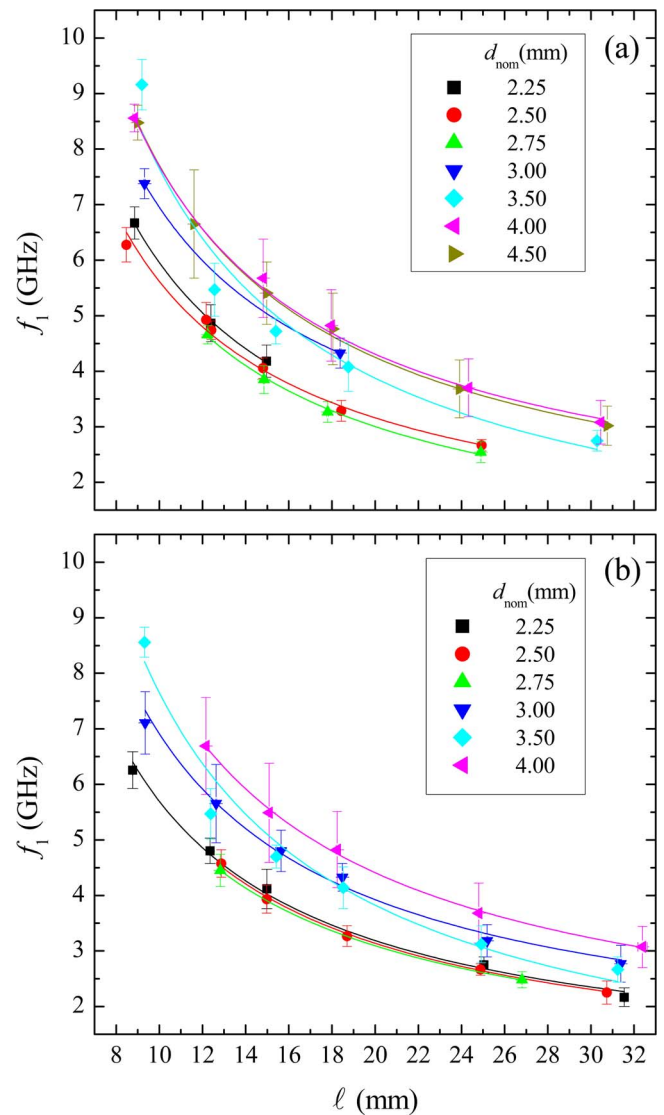


FIG. 5. Measured first order resonant frequencies as a function of ℓ for several d_{nom} values of the 31 MDS bare-metal stents (a) and the 29 MES Zotarolimus-eluting stents (b) investigated in open air. Solid lines are the least squares fits performed on each $f_1(\ell)$ data set using Eq. (4).

3.D. Microwave resonance in a water phantom

To illustrate the resonances present in a typical $A(f, \varphi)$ diagram of a stent immersed in water, we have chosen a MES stent⁴⁹ with $\ell_{\text{nom}} = 14.00$ mm and $d_{\text{nom}} = 2.25$ mm. This stent was expanded up to $p_{\text{nom}} = 0.91 \pm 0.05$ MPa using the corresponding balloon catheter. Figure 10 shows such $A(f, \varphi)$ diagram. The structures appearing around 0.25 and 0.29 GHz should be considered experimental artifacts coming from resonances generated by the phantom box, since they present no angular dependence and are common to all measured stents. Beside these artifacts, the $A(f, \varphi)$ diagram shows a characteristic bilobular structure that should be ascribed to a true stent resonant frequency ($f'_1 = 0.479 \pm 0.007$ GHz). All stents characterized inside the phantom exhibit well-defined resonances similar to the one chosen to illustrate this result. Figure 11 shows the first resonant frequency measured in water (f'_1) as a function of the first resonant frequency measured

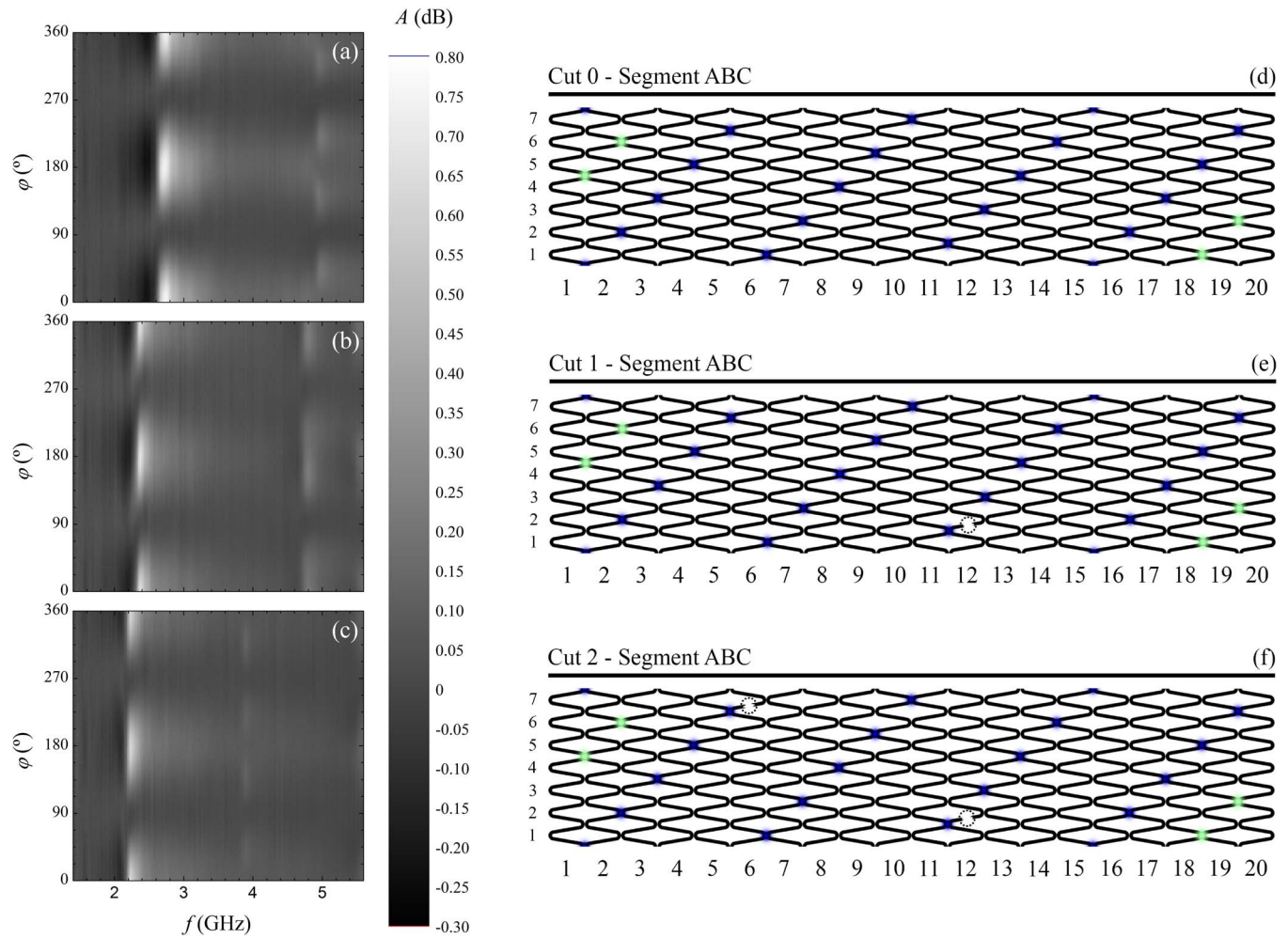


FIG. 6. (a) $A(f, \phi)$ diagram acquired in open air for a MDS bare-metal stent ($\ell_{\text{nom}} = 24.00$ mm and $d_{\text{nom}} = 2.75$ mm) expanded up to $p_{\text{nom}} = 0.91 \pm 0.05$ MPa. [(b) and (c)] Same diagrams after creating Type I and Type II fractures, respectively. [(d) and (f)] Cutting sequence performed to gradually bring the intact stent to a Type I and Type II fractured stent, respectively.

in air (f_1) for the full set of 30 MDS plus 27 MES stents tested in water.

4. DISCUSSION

4.A. Microwave resonance in open air

The shapes of the $A(\phi)$ experimental curves in Fig. 4(d) closely resemble gain patterns of a center-feed half-wave dipole antenna.⁶⁵ This fact suggests that the microwave scattering of stents is similar to that produced by such devices. Chow *et al.* have evaluated the use of stents as antennas for implantable wireless medical applications,⁶⁶ which reinforces this hypothesis. The microwave electromagnetic field couples here to the dipole antenna conductive structure and induces a standing electric current along it. As a consequence, the scattering is enhanced at resonant frequencies given by⁶⁷

$$f_n(L) = \frac{nc}{2L\sqrt{\epsilon_r\mu_r}}, \quad (3)$$

where ϵ_r and μ_r are, respectively, the relative permittivity and relative permeability of the dipole antenna surrounding medium, c is the speed of light in vacuum, L is the length of

the antenna, and n is the resonance mode. Recently, Daschner *et al.* have explained this phenomenon in the analogous context of transmission line resonators.⁶⁸

The following least squares fit⁶⁰ was performed on the $f_1(\ell)$ data set obtained for each d_{nom} value:

$$f_1(\ell) = \frac{A}{\ell} + B, \quad (4)$$

where A and B are the fitting parameters. Figures 5(a) and 5(b) represent these fits and the corresponding results are summarized in Table IV. Despite not being able to give an interpretation of B beyond its pure empirical sense, the results suggest that the resonant frequencies in a stent of a certain length are lower than those corresponding to a dipole antenna of the same length. This means that metallic stents of length ℓ should behave akin to dipole antennas of length $L = a\ell$ in terms of microwave scattering, where $a = nc/2A\sqrt{\epsilon_r\mu_r}$ is a scaling factor that can be obtained from the fit. The presence of a scaling factor greater than 1 (see a values in Table IV) should be considered reasonable because of the characteristic folded structure of coronary stents.

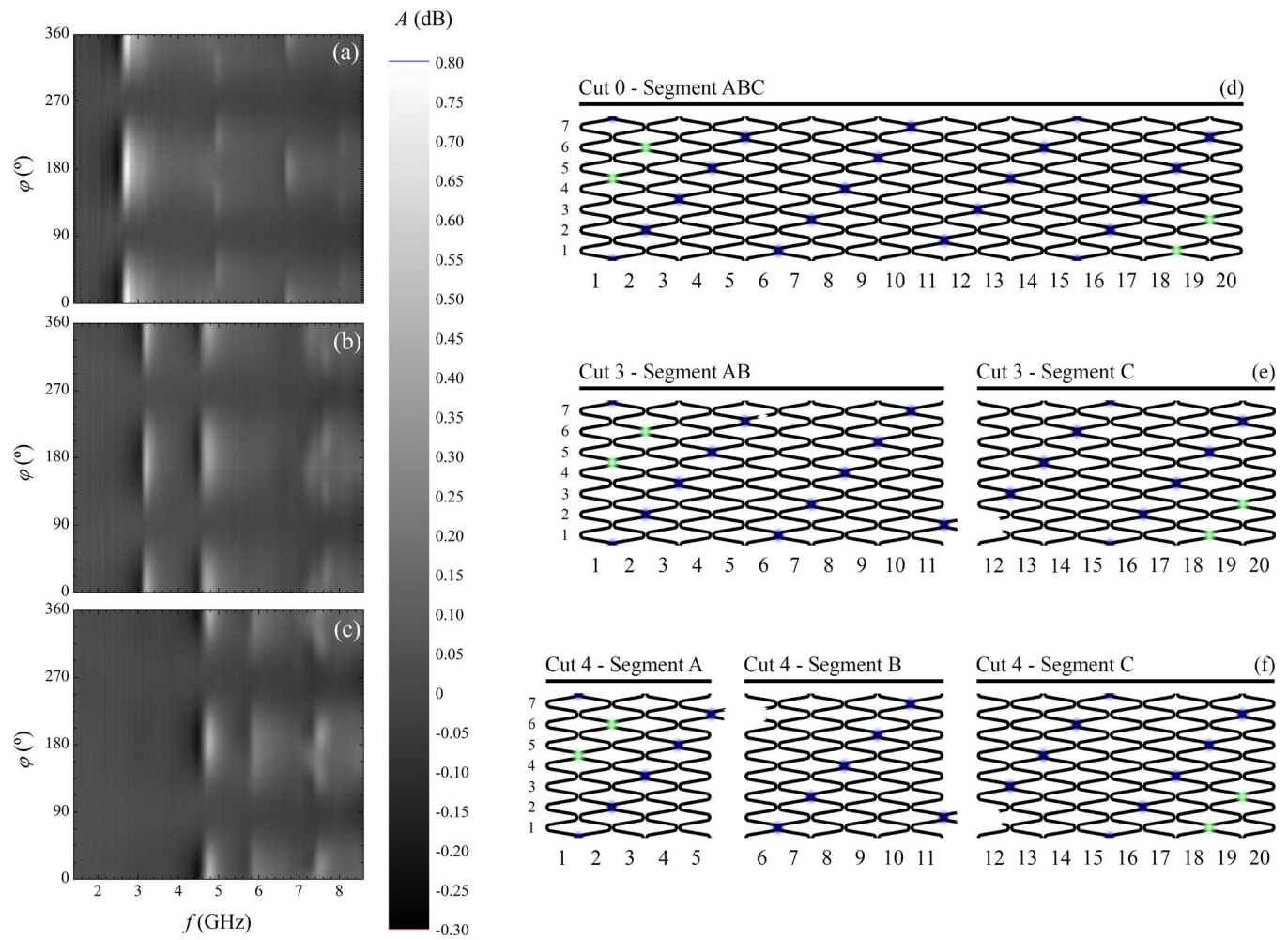


FIG. 7. (a) $A(f, \varphi)$ diagram acquired in open air for a MDS bare-metal stent ($\ell_{\text{nom}} = 24.00$ mm and $d_{\text{nom}} = 2.75$ mm) expanded up to $p_{\text{nom}} = 0.91 \pm 0.05$ MPa. [(b) and (c)] Same diagrams after creating Type III and Type IV fractures, respectively. (d) Planar representation of the original, unaltered stent. [(e) and (f)] Cutting sequence performed to gradually bring the stent from Type II to Type III and Type IV fractures, respectively.

Due to the intricate anatomy of coronary arteries, it is appropriate to discuss how the $A(f, \varphi)$ diagrams should reshape if we would measure stents presenting smooth bendings in their geometries. In this case, the values of f_n should remain mostly unchanged because these frequencies depend mainly

TABLE III. Summary of the data obtained from the fracture test presented in Figs. 6 and 7. From left to right, columns indicate cut number, segment label, first resonant frequency (f_1), stent length measured using a digital caliper (ℓ), and stent length determined from least squares fit performed on MWS data using Eq. (4) (ℓ_{MWS}).

Cut	Segment	f_1 (GHz)	ℓ (mm)	ℓ_{MWS} (mm)
0	ABC	2.58 ± 0.15	24.91 ± 0.03	24 ± 2
1	ABC	2.27 ± 0.10	24.72 ± 0.04	28 ± 3
2	ABC	2.13 ± 0.10	24.66 ± 0.04	30 ± 3
3	AB	3.08 ± 0.12	14.40 ± 0.03	19.4 ± 1.4
	C	4.53 ± 0.19	11.17 ± 0.03	12.5 ± 0.8
4	A	7.3 ± 0.3	6.64 ± 0.02	7.5 ± 0.4
	B	5.7 ± 0.2	7.93 ± 0.05	9.7 ± 0.6
	C	4.6 ± 0.2	11.17 ± 0.03	12.4 ± 0.8

on the overall length of the stent, and only scarcely on its shape. In contrast, the $A(\varphi)$ patterns could experience major changes at the resonances. For a perfectly straight resonator, the scattering will be maximum (minimum) when its axis is parallel (perpendicular) to the electric component of the incident microwave electromagnetic field.^{65,67} For a bent resonator the scattering should decrease (increase) with respect to this maximum (minimum) value, because the projection of the electric component onto its length is reduced (increased) in relation to the electric component parallel (perpendicular) to a straight resonator. As a result, the $A(\varphi)$ diagrams would soften their dependence on φ and therefore the lobes shown in Fig. 4(d) should tend gradually to become isotropic circular patterns.

4.B. Fracture tests

Figure 6 shows that Type I and Type II fractures result in a downshift of f_1 with respect to the value for the unaltered stent (see the corresponding numbers in Table III). According to Eq. (3), one might think that this decrease could be due to an eventual increase of ℓ caused by mechanical stress during

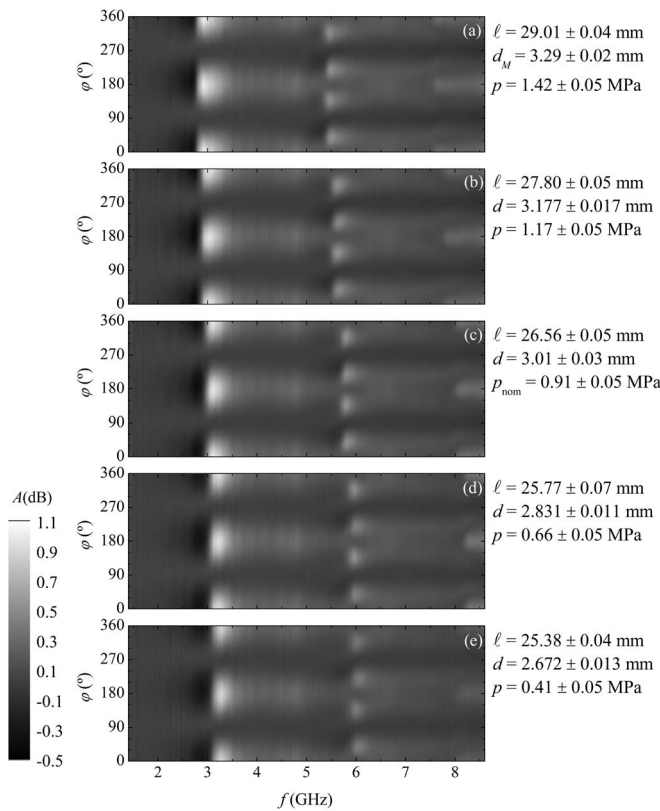


FIG. 8. (a) $A(f, \varphi)$ diagram acquired in open air for a MI bare-metal stent ($\ell_{\text{nom}} = 26.00$ mm and $d_{\text{nom}} = 2.75$ mm) expanded up to $p = 1.42 \pm 0.05$ MPa. At this stage there is no recoil, $r = 0.000 \pm 0.015$. [(b)–(e)] $A(f, \varphi)$ diagrams for increasing recoil degrees: from top to bottom, $r = 0.053 \pm 0.013$, $r = 0.133 \pm 0.015$, $r = 0.214 \pm 0.011$, and $r = 0.288 \pm 0.012$. For each stage, the real length (ℓ), the real diameter (d), and the inflation pressure (p) applied to the stent are shown.

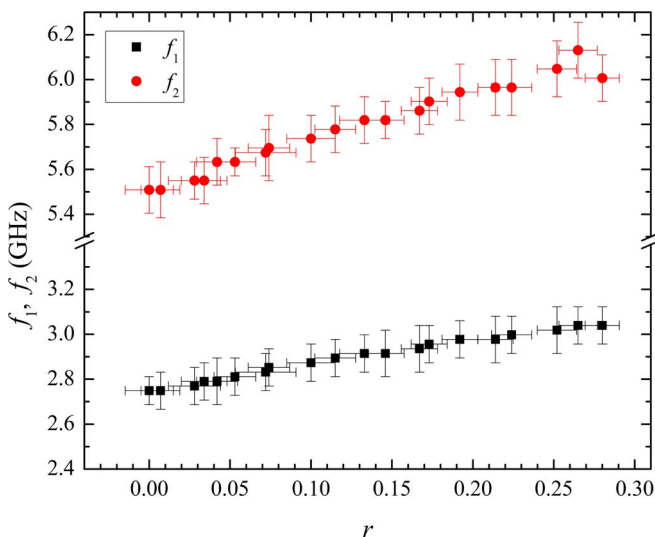


FIG. 9. First and second resonant frequencies, f_1 and f_2 , of a MI bare-metal stent ($\ell_{\text{nom}} = 26.00$ mm and $d_{\text{nom}} = 2.75$ mm) as a function of the recoil degree, r , reached by expanding the stent following a series of increasing values of the inflation pressure, p .

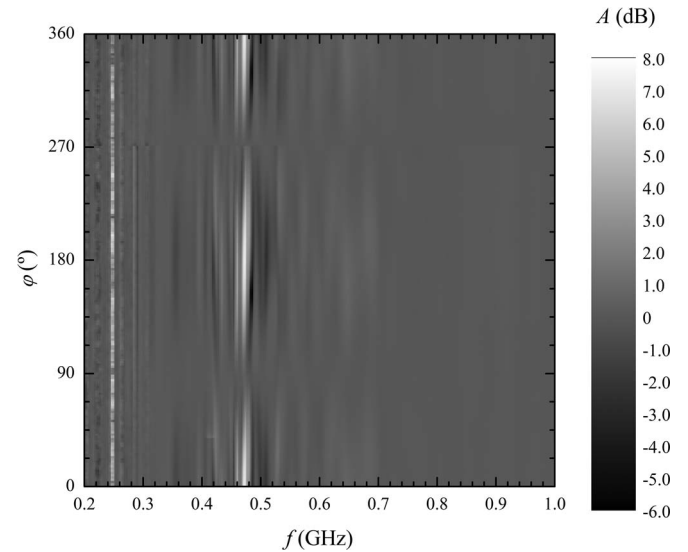


FIG. 10. $A(f, \varphi)$ diagram of a MES drug-eluting stent ($\ell_{\text{nom}} = 14.00$ mm and $d_{\text{nom}} = 2.25$ mm) expanded up to $p_{\text{nom}} = 0.91 \pm 0.05$ MPa obtained in water bath conditions.

the cutting process, but this can be disregarded by checking that Cut 1 and Cut 2 caused indeed a slight decrease instead of an increase of ℓ , as it can be seen in Table III, where ℓ diminishes from 24.91 ± 0.03 mm, for the intact stent, to 24.66 ± 0.04 mm, for the stent with two cuts. Our hypothesis is that the natural path followed by the current induced along the stent is truncated and the current is therefore compelled to take another way larger than the original, which results in a downshift of the resonant frequencies. In any case, MWS is only able to provide signs of presence of Type I and Type II fractures and not a quantitative assessment of the precise place where fractures have occurred.

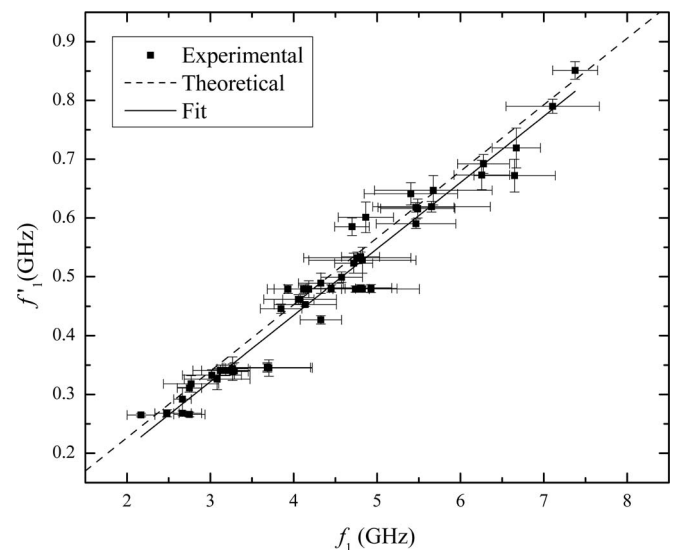


FIG. 11. Relation between the first resonant frequencies obtained experimentally for the 30 MDS plus 27 MES stents measured in water (f'_1) and in open air (f_1) conditions. The solid line represents the least squares fit performed on the $f'_1(f_1)$ data using Eq. (6). The dashed line represents the theoretical relation obtained from Eq. (5).

TABLE IV. Results of the $f_1(\ell) = A/\ell + B$ fits obtained from each $f_1(\ell)$ data set presented in Figs. 5(a) and 5(b). From left to right, columns indicate stent model, nominal size (d_{nom}), regression coefficients (A , B , r^2), and scaling factor (a). Because only two stents were available for the $d_{\text{nom}} = 3.00$ mm MDS and $d_{\text{nom}} = 2.75$ mm MES families, the values provided for these stents are just an interpolation and therefore lack error propagation analysis.

Model	d_{nom} (mm)	A (GHz mm)	B (GHz)	r^2	a
MDS	2.25	54.2 ± 1.4	0.53 ± 0.13	0.9986	2.76 ± 0.07
	2.50	49.2 ± 1.9	0.70 ± 0.12	0.993	3.08 ± 0.12
	2.75	51.3 ± 1.8	0.44 ± 0.12	0.996	2.92 ± 0.10
	3.00	58	1.2	...	2.6
	3.50	75 ± 9	0.1 ± 0.5	0.95	2.0 ± 0.2
	4.00	67.7 ± 1.1	0.93 ± 0.10	0.9989	2.22 ± 0.04
	4.50	69.2 ± 0.7	0.79 ± 0.05	0.9995	2.17 ± 0.02
MES	2.25	50 ± 2	0.68 ± 0.12	0.994	2.99 ± 0.12
	2.50	49.9 ± 1.3	0.64 ± 0.07	0.997	3.00 ± 0.08
	2.75	48	0.7	...	3.1
	3.00	60 ± 3	0.94 ± 0.19	0.98	2.51 ± 0.14
	3.50	77 ± 6	0.0 ± 0.4	0.97	1.96 ± 0.14
	4.00	70.5 ± 1.4	0.89 ± 0.07	0.998	2.13 ± 0.04

Figure 7(c) shows that in a Type III fracture the characteristic f_1 resonance of the unaltered stent ($f_1^{0ABC} = 2.58 \pm 0.15$ GHz) disappears and two new f_1 modes occur at higher frequencies, one for each emerging segment ($f_1^{3AB} = 3.08 \pm 0.12$ GHz and $f_1^{3C} = 4.53 \pm 0.19$ GHz). From these new frequencies and using the $f_1(\ell)$ fit parameters obtained for the $d_{\text{nom}} = 2.75$ mm MDS stent family, we can estimate via Eq. (4) the corresponding lengths of such new segments, ℓ_{MWS} (fifth column in Table III). Similarly, Fig. 7(e) shows that after applying Cut 4 on segment AB, its corresponding resonance splits again in two new f_1 modes of even higher frequencies ($f_1^{4A} = 7.3 \pm 0.3$ GHz and $f_1^{4B} = 5.7 \pm 0.2$ GHz). Notice how the resonance for segment C remains unchanged ($f_1^{4C} = 4.6 \pm 0.2$ GHz). Although ℓ_{MWS} values are not compatible with those obtained from direct measurement using a digital caliper (fourth column in Table III), we demonstrate here that a rough quantitative assessment of the length of each segment is possible. Moreover, the presence of Type III or Type IV fractures can be simply reported from a qualitative inspection of the $A(f, \varphi)$ diagrams provided by MWS.

4.C. Recoil tests

Results obtained in recoil tests are more subtle than those achieved in fracture tests. On the one hand, the link between the recoil experienced by a stent and its characteristic resonant frequencies is rather indirect. Recoil results in a slight rise of the resonant frequencies only if it involves reduction of the stent length. In other words, if a certain recoil process maintains the original stent length, it should not modify the shape of the corresponding $A(f, \varphi)$ diagram and therefore would not be detected by MWS. In any case, in other stents submitted to the same test, the link between longitudinal shrinkage and recoil seems to be a common feature. On the other hand, the

fact that $f_2(r)$ increases faster than $f_1(r)$ (see Fig. 9) is in accordance with the linear dependence of f_n on the resonant mode n as it appears in Eq. (3).

More complex situations, such as partial recoil affecting just a segment of the stent length, should also be detectable by means of MWS, but only if the associated overall shortening is enough to reshape the corresponding $A(f, \varphi)$ diagram. For a given recoil-related shrinkage, the shorter the stent is, the more significant the corresponding rise of the resonant frequency will be. This can be understood taking into account the characteristic $1/\ell$ behavior of the stent resonant frequencies, since $f_n(\ell)$ varies faster for low ℓ values than for high values [see for instance $f_1(\ell)$ in Fig. 5]. Nonetheless, MWS cannot give a hint of the precise place where this nonuniform recoil would occur.

4.D. Microwave resonance in a water phantom

The main characteristic that can be noticed in Fig. 10 is that the resonance that appears in the $A(f, \varphi)$ diagram ($f'_1 = 0.479 \pm 0.007$ GHz) is shifted 1 order of magnitude down with respect to the one obtained for the same stent in open air ($f_1 = 4.1 \pm 0.4$ GHz). Notwithstanding, the resonances of the shortest stents usually appear quite blurry when compared with those of the largest ones, and they may be difficult to detect. Additionally, none of the $A(f, \varphi)$ diagrams acquired provides traces of the second resonant modes predicted by Eq. (3).

In order to check if the downshift mentioned before is in line with theoretical expectations, we can use Eq. (3) to obtain a general relation linking the frequency values in two dielectric media:

$$f'_n = f_n \sqrt{\frac{\epsilon_r \mu_r}{\epsilon'_r \mu'_r}}. \quad (5)$$

Assuming air ($\epsilon_r \approx 1$, $\mu_r \approx 1$) and water ($\epsilon'_r \approx 78$, $\mu'_r \approx 1$) as initial and final medium, respectively, and considering that the parameters for water are practically constant between 0.1 and 1.0 GHz,⁶¹ the relation $f'_n \approx f_n/\sqrt{78}$ should hold theoretically.

The following least squares fit⁶⁰ was then performed on the $f'_1(f_1)$ data set shown in Fig. 11:

$$f'_1(f_1) = A' f_1 + B', \quad (6)$$

where $A' = 0.113 \pm 0.004$ and $B' = -0.017 \pm 0.016$ GHz are the values obtained for the fitting parameters. The corresponding fit (solid line) as well as the theoretical $f'_1(f_1)$ dependence predicted (dashed line) are depicted in Fig. 11 together with the experimental data. Although the points in this figure are somewhat scattered, the fit provides a good agreement with the theoretical line ($r^2 = 0.95$). Moreover, implicit in this accordance is the fact that the f'_1 values in water do also respect the characteristic $1/\ell$ law followed by the corresponding f_1 values in open air (Fig. 5).

4.E. Final considerations

The experiments described in this paper are only intended to establish properties of cardiovascular stents, and the experimental setups used may not be representative of future equipment to be used in clinical practice. Our setups are conceptually derived from the ones used in measurements done for radar target characterization,^{69,70} where antennas are placed in a far field regime.⁶⁷ As a result, the receiving antenna gathers a significant amount of stray signals besides the ones scattered by the stent. In a clinical environment these stray signals would be predominantly produced by scattering in surrounding tissues and bones and may be strong enough to mask the signal scattered by the stent. We foresee two possible alternatives to circumvent this.

The first one would consist in using near-field probes instead of antennas, so that the microwave electric and magnetic fields would be spatially confined to a small region around the stent. The second alternative would consist in the usage of modern microwave imaging techniques.^{71,72} These techniques are capable of resolving spatially the scattering produced at different points of the scanned volume, and could be used to isolate the scattering produced by the stent from that produced by surrounding tissues and bones. This capacity is limited by the size of the resolution bins (voxels) of the imaging technique, which depends on the wavelength in the medium and the imaging algorithm used. While most of these techniques use single frequency illumination, some broadband alternatives have been developed in recent years (see Ref. 72 and references therein). Hence, these imaging techniques could be used to evaluate the frequency response of the scattered fields at the voxel(s) containing the stent to monitor its structural integrity. In other words, our work shows that these imaging techniques do not need to achieve an imaging resolution capable of distinguishing the features to be detected (fracture, recoil, shortening, etc.), as long as they cover a frequency spectrum which is wide enough to detect the frequency shifts provided by these features, either at their fundamental frequency or at one of its higher-order resonances.

Any of the two alternatives above would have to cope with the signal fluctuation due to physiological motion such as breath or heartbeat.⁷³ To achieve this, a clinical apparatus should use short acquisition times for the elemental measurement events. Multiple measurement events may then be averaged to improve the signal to noise ratio provided that the measurements are synchronized with the heart rate.⁷⁴

5. CONCLUSION

We have proved experimentally that metallic coronary stents of millimeter size exhibit characteristic resonant frequencies in their open air microwave scattering spectra. The presence of such resonances could be understood using a simple theoretical model based on dipole antennas. We have also tested the ability of our approach for the detection of stent structural distortions. Microwave spectrometry provides signs of presence of stent fractures ranging from Type I to Type IV. Despite achieving only a qualitative assessment for Type

I and Type II fractures, a quantitative evaluation of Type III and Type IV fractures is feasible. The method appears less effective detecting stent recoil, but its quantitative evaluation seems also possible if the diametrical shrinkage involves longitudinal shortening. Finally, preliminary tests using a water-based phantom to simulate tissue have been performed. In addition to observing the resonant frequencies of stents submerged within the phantom, the results are in fair agreement with theoretical estimates.

All this encourages to continue investigating, but much remains to be done. In the first place, experiments should go on by reproducing fracture and recoil test results in a more reliable physiological phantom, and by extending the work using *ex vivo* and *in vivo* trials in animal models. Moreover, there is work pending in regard to the study of more complex geometrical distortions, such as Type V fractures and nonuniform recoil, as well as to the investigation of recently observed failure modes in coronary stents, such as longitudinal compression or postdeployment shortening.^{75,76} Finally, in the frequency range where we expect to find resonances in implanted stents (0.2–2.0 GHz), the values of relative permittivity for blood and smooth muscle cells (the major component in typical neointimal hyperplasia) are different enough⁷⁷ as to provoke a frequency shift in the stent resonances. This would mean that the presence of restenosis could be potentially detected by MWS. We are focusing efforts on these prospects, because we understand restenosis as the ultimate goal MWS should address.

ACKNOWLEDGMENTS

G.A.-G. and J.T. thank *ICREA Acadèmia* and *Universitat de Barcelona* for financial support. O.R.-L. and A.B.-G. thank Medtronic for providing the stents studied in the present work. J.M.O'C. thanks the Spanish Government Project No. MAT2011-29269-C03-02. A.G.-S. thanks *Universitat de Barcelona* for backing his research.

^{a)} gian.arauz@ub.edu

^{b)} Author to whom correspondence should be addressed. Electronic mail: agarciasan@ub.edu

¹ S. Garg and P. W. Serruys, "Coronary stents: Looking forward," *J. Am. Coll. Cardiol.* **56**, S43–S78 (2010).

² S. Garg and P. W. Serruys, "Coronary stents: Current status," *J. Am. Coll. Cardiol.* **56**, S1–S42 (2010).

³ R. Schatz, J. Palmaz, F. Tio, F. Garcia, O. Garcia, and S. Reuter, "Balloon-expandable intracoronary stents in the adult dog," *Circulation* **76**, 450–457 (1987).

⁴ S. P. Karas, M. B. Gravanis, E. C. Santoian, K. A. Robinson, K. A. Anderberg, and S. B. King III, "Coronary intimal proliferation after balloon injury and stenting in swine: An animal model of restenosis," *J. Am. Coll. Cardiol.* **20**, 467–474 (1992).

⁵ P. C. Gordon, C. Gibson, D. J. Cohen, J. P. Carrozza, R. E. Kuntz, and D. S. Baim, "Mechanisms of restenosis and redilation within coronary stents—Quantitative angiographic assessment," *J. Am. Coll. Cardiol.* **21**, 1166–1174 (1993).

⁶ R. Hoffmann, G. S. Mintz, G. R. Dussallant, J. J. Popma, A. D. Pichard, L. F. Satler, K. M. Kent, J. Griffin, and M. B. Leon, "Patterns and mechanisms of in-stent restenosis," *Circulation* **94**, 1247–1254 (1996).

⁷ D. J. Moliterno, "Healing Achilles—Sirolimus versus paclitaxel," *N. Engl. J. Med.* **353**, 724–727 (2005).

- ⁸G. G. Stefanini and D. R. Holmes, "Drug-eluting coronary-artery stents," *N. Engl. J. Med.* **368**, 254–265 (2013).
- ⁹C. Stettler, S. Wandel, S. Allemann, A. Kastrati, M. C. Morice, A. Schömig, M. E. Pfisterer, G. W. Stone, M. B. Leon, J. S. de Lezo, J.-J. Goy, S.-J. Park, M. Sabaté, M. J. Suttorp, H. Kelbaek, C. Spaulding, M. Menichelli, P. Vermeersch, M. T. Dirksen, P. Cervinka, A. S. Petronio, A. J. Nordmann, P. Diem, B. Meier, M. Zwahlen, S. Reichenbach, S. Trelle, S. Windecker, and P. Jüni, "Outcomes associated with drug-eluting and bare-metal stents: A collaborative network meta-analysis," *Lancet* **370**, 937–948 (2007).
- ¹⁰C. Spaulding, J. Daemen, E. Boersma, D. E. Cutlip, and P. W. Serruys, "A pooled analysis of data comparing sirolimus-eluting stents with bare-metal stents," *N. Engl. J. Med.* **356**, 989–997 (2007).
- ¹¹G. W. Stone, J. W. Moses, S. G. Ellis, J. Schofer, K. D. Dawkins, M.-C. Morice, A. Colombo, E. Schampaert, E. Grube, A. J. Kirtane, D. E. Cutlip, M. Fahy, S. J. Pocock, R. Mehran, and M. B. Leon, "Safety and efficacy of sirolimus- and paclitaxel-eluting coronary stents," *N. Engl. J. Med.* **356**, 998–1008 (2007).
- ¹²L. Mauri, W.-h. Hsieh, J. M. Massaro, K. K. Ho, R. D'Agostino, and D. E. Cutlip, "Stent thrombosis in randomized clinical trials of drug-eluting stents," *N. Engl. J. Med.* **356**, 1020–1029 (2007).
- ¹³A. Kastrati, J. Mehilli, J. Pache, C. Kaiser, M. Valgimigli, H. Kelbaek, M. Menichelli, M. Sabaté, M. J. Suttorp, D. Baumgart, M. Seyfarth, M. E. Pfisterer, and A. Schömig, "Analysis of 14 trials comparing sirolimus-eluting stents with bare-metal stents," *N. Engl. J. Med.* **356**, 1030–1039 (2007).
- ¹⁴F. Amico, S. Geraci, and C. Tamburino, "Acute coronary syndrome due to early multiple and complete fractures in sirolimus-eluting stent: A case report and brief literature review," *Catheter. Cardiovasc. Interv.* **81**, 52–56 (2013).
- ¹⁵H. Ben-Salem, M. Kamoun, H. Khaldi, K. Ghannem, S. Majadla, M. Ghannem, and S. Godard, "Sirolimus-eluting stent displaced fracture: Case report and review of the literature," *Ann. Cardiol. Angiol.* **61**, 64–68 (2012).
- ¹⁶S. W. Lee, F. C. Tam, and K. K. Chan, "Very late stent thrombosis due to DES fracture: Description of a case and review of potential causes," *Catheter. Cardiovasc. Interv.* **78**, 1101–1105 (2011).
- ¹⁷A. Lousinha, A. Fiarresga, L. Cardona, J. P. Lopes, A. Lopes, D. Cacula, L. de Sousa, L. Patrício, L. Bernardes, and R. C. Ferreira, "Stent fracture: Case report and literature review," *Rev. Port. Cardiol.* **30**, 213–221 (2011).
- ¹⁸B. Kapoor, M. Lockhart, D. Sharma, and I. D. Maya, "Brachiocephalic vein stent fracture: Case series and literature review," *Semin. Dialysis* **23**, 110–113 (2010).
- ¹⁹H. Tizón-Marcos, R. de Larochelière, and E. Larose, "Breakpoint: Left main stent fracture—Review of the literature," *J. Interv. Cardiol.* **22**, 362–367 (2009).
- ²⁰S.-K. Chua and H.-F. Hung, "Renal artery stent fracture with refractory hypertension: A case report and review of the literature," *Catheter. Cardiovasc. Interv.* **74**, 37–42 (2009).
- ²¹T. Koh and A. Mathur, "Coronary stent fracture in a saphenous vein graft to right coronary artery—Successful treatment by the novel use of the Jomed coronary stent graft: Case report and review of the literature," *Int. J. Cardiol.* **119**, e43–e45 (2007).
- ²²T. Canan and M. S. Lee, "Drug-eluting stent fracture: Incidence, contributing factors, and clinical implications," *Catheter. Cardiovasc. Interv.* **75**, 237–245 (2010).
- ²³G. S. Sfyroeras, A. Koutsiaris, C. Karathanos, A. Giannakopoulos, and A. D. Giannoukas, "Clinical relevance and treatment of carotid stent fractures," *J. Vasc. Surg.* **51**, 1280–1285 (2010).
- ²⁴A. K. Chhatrwalla, A. Cam, S. Unzek, D. L. Bhatt, R. E. Raymond, A. M. Lincoff, P. L. Whitlow, S. G. Ellis, E. M. Tuzcu, and S. R. Kapadia, "Drug-eluting stent fracture and acute coronary syndrome," *Cardiovasc. Revasc. Med.* **10**, 166–171 (2009).
- ²⁵J. Rits, J. van Herwaarden, A. Jahrome, D. Krievins, and F. Moll, "The incidence of arterial stent fractures with exclusion of coronary, aortic, and non-arterial settings," *Eur. J. Vasc. Endovasc.* **36**, 339–345 (2008).
- ²⁶T. Chakravarty, A. J. White, M. Buch, H. Naik, N. Doctor, J. Schapira, S. Kar, J. S. Forrester, R. E. Weiss, and R. Makkar, "Meta-analysis of incidence, clinical characteristics and implications of stent fracture," *Am. J. Cardiol.* **106**, 1075–1080 (2010).
- ²⁷W.-S. Chung, C.-S. Park, K.-B. Seung, P.-J. Kim, J.-M. Lee, B.-K. Koo, Y.-S. Jang, J.-Y. Yang, J.-H. Yoon, D.-I. Kim, Y.-W. Yoon, J.-S. Park, Y.-H. Cho, and S.-J. Park, "The incidence and clinical impact of stent strut fractures developed after drug-eluting stent implantation," *Int. J. Cardiol.* **125**, 325–331 (2008).
- ²⁸D. Allie, C. Hebert, and C. Walker, "Nitinol stent fractures in the SFA: The biomechanical forces exerted on the SFA provide a "stiff" challenge to endovascular stenting," *Endovasc. Today* **3**, 22–34 (2004).
- ²⁹S. Adlakha, M. Sheikh, J. Wu, M. W. Burket, U. Pandya, W. Colyer, E. Eltahawy, and C. J. Cooper, "Stent fracture in the coronary and peripheral arteries," *J. Interv. Cardiol.* **23**, 411–419 (2010).
- ³⁰K. Takagi, T. Yakushiji, S. Basavarajiah, A. Chieffo, T. Hasegawa, and A. Colombo, "Acute stent recoil from aggressive post-dilation of a second-generation drug-eluting stent," *J. Am. Coll. Cardiol. Interv.* **6**, 311–313 (2013).
- ³¹T. Tsunoda, M. Nakamura, M. Wada, N. Ito, Y. Kitagawa, M. Shiba, S. Yajima, R. Iijima, R. Nakajima, M. Yamamoto, T. Takagi, T. Yoshitama, H. Anzai, T. Nishida, and T. Yamaguchi, "Chronic stent recoil plays an important role in restenosis of the right coronary ostium," *Coronary Artery Dis.* **15**, 39–44 (2004).
- ³²M.-K. Hong, S.-W. Park, C. W. Lee, J.-Y. Ko, D.-H. Kang, J.-K. Song, J.-J. Kim, R. Hoffmann, G. S. Mintz, and S.-J. Park, "Intravascular ultrasound comparison of chronic recoil among different stent designs," *Am. J. Cardiol.* **84**, 1247–1250 (1999).
- ³³B.-K. Koo, K. Waseda, J. Ako, T. Hasegawa, T. Shimohama, D. Nakatani, H. Otake, M. Yamasaki, R. Sakurai, I. Tsujino, Y. Honda, and P. J. Fitzgerald, "Incidence of diffuse and focal chronic stent recoil after implantation of current generation bare-metal and drug-eluting stents," *Int. J. Cardiol.* **144**, 132–134 (2010).
- ³⁴G. B. Danzi, L. Fiocca, C. Capuano, S. Predolini, and E. Quaini, "Acute stent recoil: In vivo evaluation of different stent designs," *Catheter. Cardiovasc. Interv.* **52**, 147–153 (2001).
- ³⁵J. A. Ormiston and P. W. Serruys, "Bioabsorbable coronary stents," *Circ. Cardiovasc. Interv.* **2**, 255–260 (2009).
- ³⁶E. Chow, A. Chlebowski, S. Chakraborty, W. Chappell, and P. Irazoqui, "Fully wireless implantable cardiovascular pressure monitor integrated with a medical stent," *IEEE Trans. Biomed. Eng.* **57**, 1487–1496 (2010).
- ³⁷K. Takahata, Y. Gianchandani, and K. Wise, "Micromachined antenna stents and cuffs for monitoring intraluminal pressure and flow," *J. Microelectromech. Syst.* **15**, 1289–1298 (2006).
- ³⁸K. Takahata and Y. Gianchandani, "A planar approach for manufacturing cardiac stents: design, fabrication, and mechanical evaluation," *J. Microelectromech. Syst.* **13**, 933–939 (2004).
- ³⁹H. Eggebrecht, H. Kühl, G. M. Kaiser, S. Aker, M. O. Zenge, F. Stock, F. Breuckmann, F. Grabellus, M. E. Ladd, R. H. Mehta, R. Erbel, and H. H. Quick, "Feasibility of real-time magnetic resonance-guided stent-raft placement in a swine model of descending aortic dissection," *Eur. Heart J.* **27**, 613–620 (2006).
- ⁴⁰S. M. Wetzner, L. C. Kiser, and J. S. Bezreh, "Duplex ultrasound imaging: Vascular applications," *Radiology* **150**, 507–514 (1984).
- ⁴¹B. Perrenot, R. Vaillant, R. Prost, G. Finet, P. Douek, and F. Peyrin, "Motion correction for coronary stent reconstruction from rotational x-ray projection sequences," *IEEE Trans. Med. Imaging* **26**, 1412–1423 (2007).
- ⁴²S. E. Nissen and P. Yock, "Intravascular ultrasound," *Circulation* **103**, 604–616 (2001).
- ⁴³B. Wang, J. Su, A. Karpiouk, K. Sokolov, R. Smalling, and S. Emelianov, "Intravascular photoacoustic imaging," *IEEE J. Sel. Top. Quantum Electron.* **16**, 588–599 (2010).
- ⁴⁴C. Kauffmann, P. Motreff, and L. Sarry, "In vivo supervised analysis of stent reendothelialization from optical coherence tomography," *IEEE Trans. Med. Imaging* **29**, 807–818 (2010).
- ⁴⁵A. Vander Vorst, A. Rosen, and Y. Kotsuka, *RF/Microwave Interaction with Biological Tissues* (John Wiley and Sons, Inc., New Jersey, 2006).
- ⁴⁶Driver Sprint Rapid Exchange Coronary Stent System Instructions for Use, *Medtronic, Inc.*, Minneapolis, MN, USA.
- ⁴⁷Integrity Rapid Exchange Coronary Stent System Instructions for Use, *Medtronic, Inc.*, Minneapolis, MN, USA.
- ⁴⁸Driver & Micro-Driver Rapid Exchange Coronary Stent System Instructions for Use, *Medtronic, Inc.*, Minneapolis, MN, USA.
- ⁴⁹Endeavor Sprint Zotarolimus-Eluting Rapid Exchange Coronary Stent System Instructions for Use, *Medtronic, Inc.*, Minneapolis, MN, USA.
- ⁵⁰Endeavor Resolute Zotarolimus-Eluting Rapid Exchange Coronary Stent System Instructions for Use, *Medtronic, Inc.*, Minneapolis, MN, USA.
- ⁵¹Rapid Exchange Stent Delivery System, *Medtronic, Inc.*, Minneapolis, MN.

- ⁵²Encore 26 Advantage Kit, *Boston Scientific, Corp.*, Natick, MA, USA.
- ⁵³Digital Micro-measure Camera BW-400X, *Premier Farnell, Plc.*, London, UK.
- ⁵⁴JXTXLX-20180, *Chengdu A-info Inc.*, Chengdu, China.
- ⁵⁵HP 8510C, *Agilent Technologies*, Santa Clara, CA.
- ⁵⁶Sub-Miniature version A 3GW40-0TD01D02048.0, *W.L. Gore & Associates Inc.*, Newark, DE.
- ⁵⁷ST2818M1006-B, *Nanotec Electronic GmbH & Co. KG*, Munich, Germany.
- ⁵⁸Arduino Uno, *Interaction Design Institute Ivrea*, Ivrea, TO, Italy.
- ⁵⁹LabVIEW 8.5, *National Instruments Corp.*, Austin, TX.
- ⁶⁰OriginPro 8 SRO, *OriginLab Corp.*, Northampton, MA.
- ⁶¹W. Ellison, K. Lamkaouchi, and J.-M. Moreau, "Water: A dielectric reference," *J. Mol. Liq.* **68**, 171–279 (1996).
- ⁶²*Vogel Germany*, Kvelaer, Nordrhein-Westfalen, Germany.
- ⁶³M. Jaff, M. Dake, J. Pompa, G. Ansel, and T. Yoder, "Standardized evaluation and reporting of stent fractures in clinical trials of noncoronary devices," *Catheter. Cardiovasc. Interv.* **70**, 460–462 (2007).
- ⁶⁴See supplementary material at <http://dx.doi.org/10.1118/1.4866881> for the $f_1(d)$ dependence for several ℓ_{nom} values, and the $f_2(\ell)$ dependence for several d_{nom} values.
- ⁶⁵S. J. Orfanidis, *Electromagnetic Waves and Antennas* (Rutgers University, New Jersey, 2002).
- ⁶⁶E. Chow, Y. Ouyang, B. Beier, W. Chappell, and P. Irazoqui, "Evaluation of cardiovascular stents as antennas for implantable wireless applications," *IEEE Trans. Microwave Theory Tech.* **57**, 2523–2532 (2009).
- ⁶⁷C. A. Balanis, *Antenna Theory: Analysis and Design* (Wiley, New York, 1997).
- ⁶⁸F. Daschner, S. Hoffmann, R. Knochel, M. Jerosch-Herold, and C. Rickers, "Resonant stents for non-invasive monitoring of restenosis," in *2011 41st European Microwave Conference (EuMC)* (IEEE, Manchester, 2011), pp. 972–975.
- ⁶⁹M. I. Skolnik, *Introduction to Radar Systems* (McGraw-Hill, New York, 2001).
- ⁷⁰"IEEE Standard Radar Definitions," IEEE Std 686-1997, 1–41 (1998).
- ⁷¹M. Guardiola, S. Capdevila, J. Romeu, and L. Jofre, "3-D microwave magnitude combined tomography for breast cancer detection using realistic breast models," *Antennas Wireless Propag. Lett. IEEE* **11**, 1622–1625 (2012).
- ⁷²M. Guardiola, S. Capdevila, S. Blanch, J. Romeu, and L. Jofre, "UWB high-contrast robust tomographic imaging for medical applications," in *International Conference on Electromagnetics in Advanced Applications, 2009 (ICEAA'09)* (IEEE, Torino, 2009), pp. 560–563.
- ⁷³L. Changzhi, J. Cummings, J. Lam, E. Graves, and W. Wu, "Radar remote monitoring of vital signs," *Microwave Mag. IEEE* **10**, 47–56 (2009).
- ⁷⁴L. B. Da Silva, V. C. Esch, A. M. Rubenchik, J. Hares, J. D. Kilkenny, G. W. Collins, and P. J. Weber, "In-stent restenosis detection device," US6729336 B2 Patent (04 May 2003).
- ⁷⁵C. Hanratty and S. Walsh, "Longitudinal compression: A "new" complication with modern coronary stent platforms—Time to think beyond deliverability?" *Eurointervention* **7**, 872–877 (2011).
- ⁷⁶P. Mortier and M. De Beule, "Stent design back in the picture: An engineering perspective on longitudinal stent compression," *Eurointervention* **7**, 773–775 (2011).
- ⁷⁷S. Gabriel, R. W. Lau, and C. Gabriel, "The dielectric properties of biological tissues. III. Parametric models for the dielectric spectrum of tissues," *Phys. Med. Biol.* **41**, 2271–2293 (1996).